Supplements

Exploring the causes of multicentury pluvials in the Altiplano with a climate modeling experiment

Ignacio A. Jara[a], Orlando Astudillo[b], Pablo Salinas[b], Limbert Torrez-Rodriguez[b,c], Nicolás Lampe[d], Antonio Maldonado[b,e]

[a.] Departamento de Ciencias Históricas y Geográficas, Universidad de Tarapacá, Arica, Chile

[b.] Centro de Estudios Avanzados en Zonas Áridas (CEAZA), Colina del Pino, La Serena, Chile

[c.] Universidad de La Serena, La Serena, Chile

[d.] Departamento de Ingeniería en Computación e Informática, Facultad de Ingeniería, Universidad de Tarapacá, Arica Chile

[e.] Departamento de Biología Marina, Universidad Católica del Norte, Coquimbo, Chile

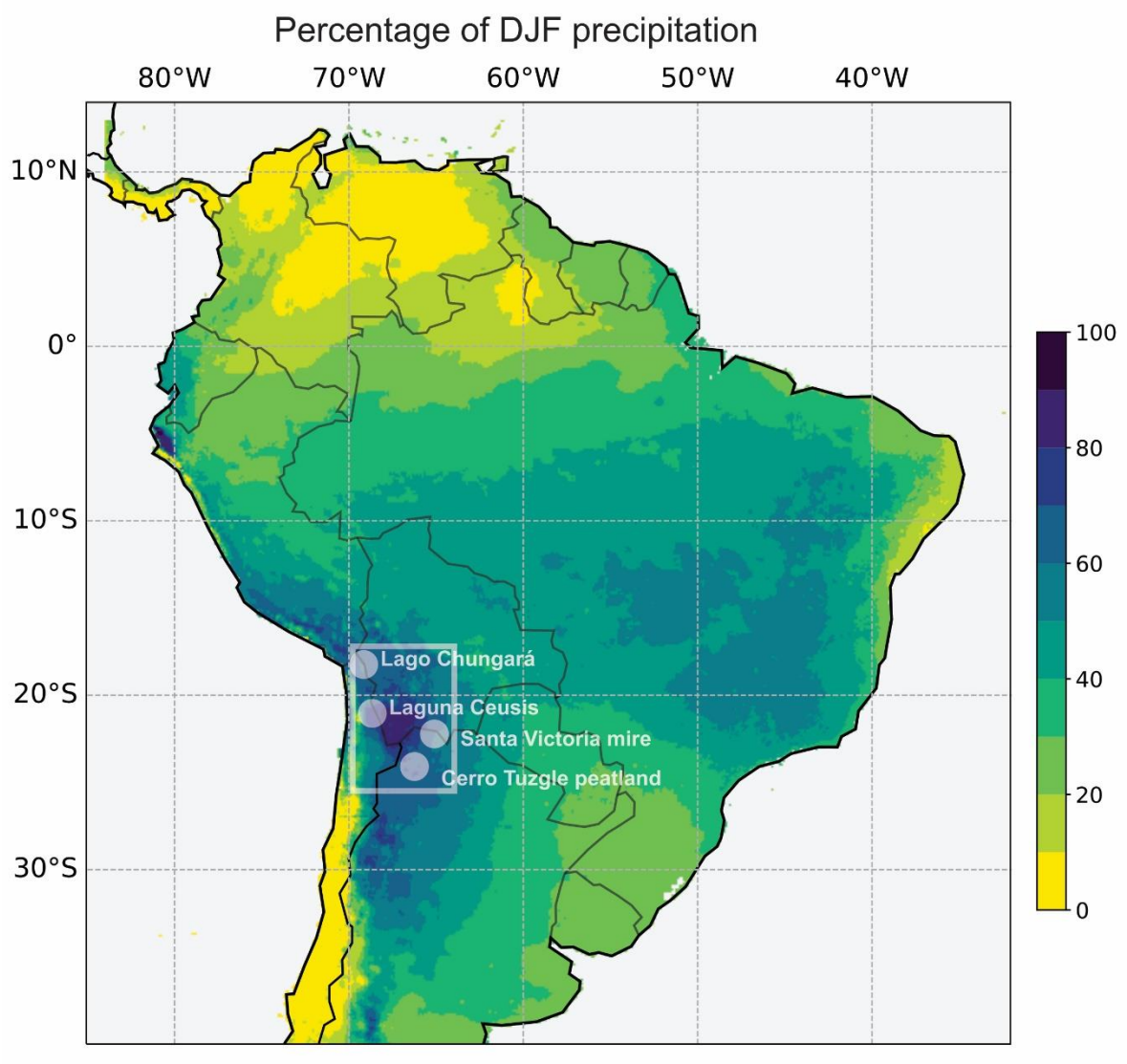

Figure S1. Percentage of DJF precipitation in South America, including the location of the proxy records presented in the main text: Laguna Ceusis (Jara et al., 2020), Lago Chungará (Jara et al., 2019), Santa Victoria mire (Hooper et al., 2020) and Cerro Tuzgle (Kock et al., 2019). The southern Altiplano is demarked by the white rectangle. Precipitation data correspond to ERA5 Reanalysis.

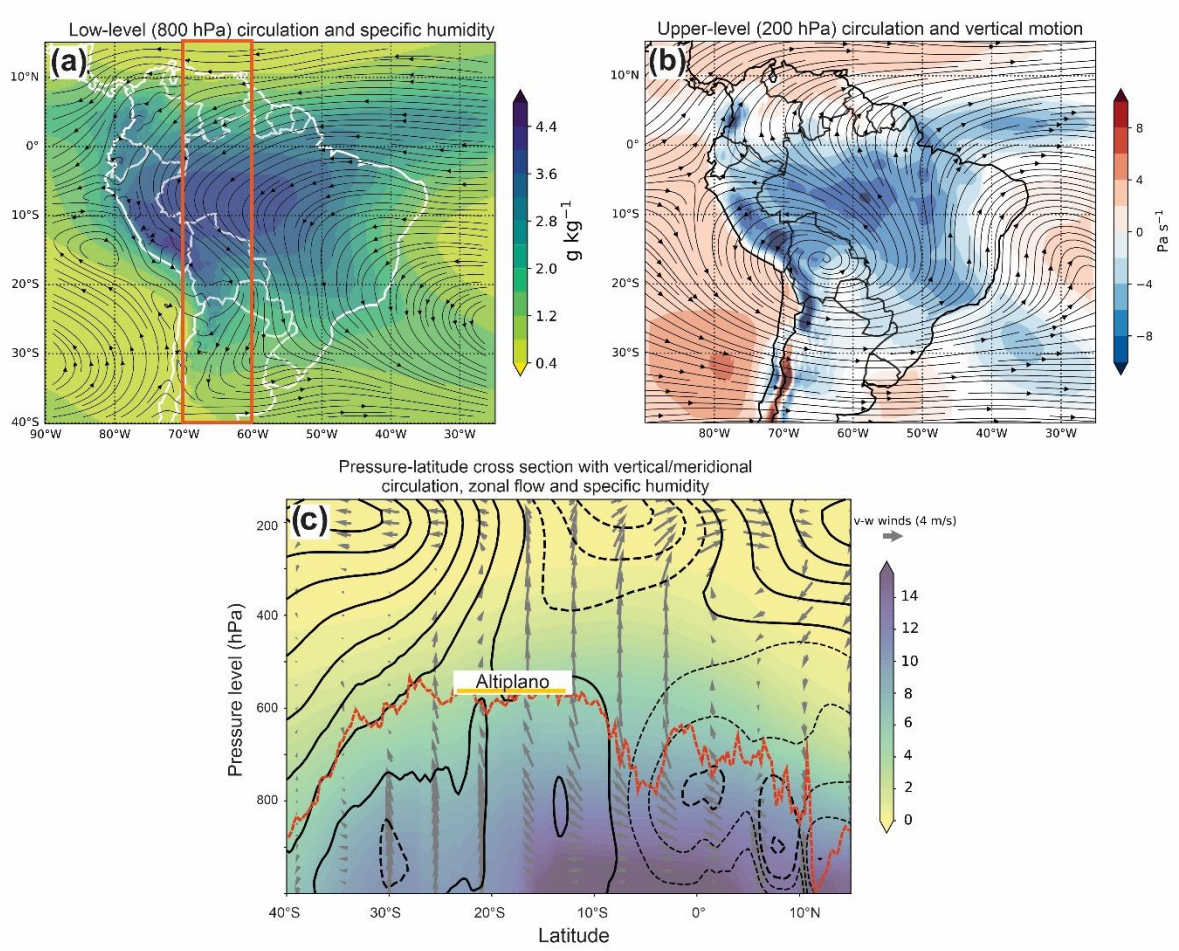

Figure S2. 1951–2022 South America DJF climatology. **(a)** Specific humidity (q) at 500 hPa (shaded; g kg^{-1}) along with integrated zonal and meridional winds at 800 hPa (streamlines). **(b)** Vertical motion (w) at 500 hPa (shaded; Pa s−1) and integrated zonal and meridional winds (u,v) at 200 hPa (streamlines). Upward (downward) motion is depicted as negative blue (positive red) values. **(c)** Pressure-latitude cross section showing the integrated vertical and meridional circulation (v,w; vectors; m s^{-1}), zonal winds (u; contours), and specific humidity (q; shaded). The longitudinal means are calculated using v, w, u and q within the region delimited by the red rectangle in (a). Westerly (easterly) circulation is depicted as continuous (dashed) lines, with label at 4 m s^{-1} intervals. The dashed red line of the image represents the profile of maximum elevation of the Andes cordillera along the red rectangles in (b), calculated as the maximum topographic elevation. The position of the Altiplano is labelled in the figure (c). All atmospheric data correspond to ERA5 reanalysis.

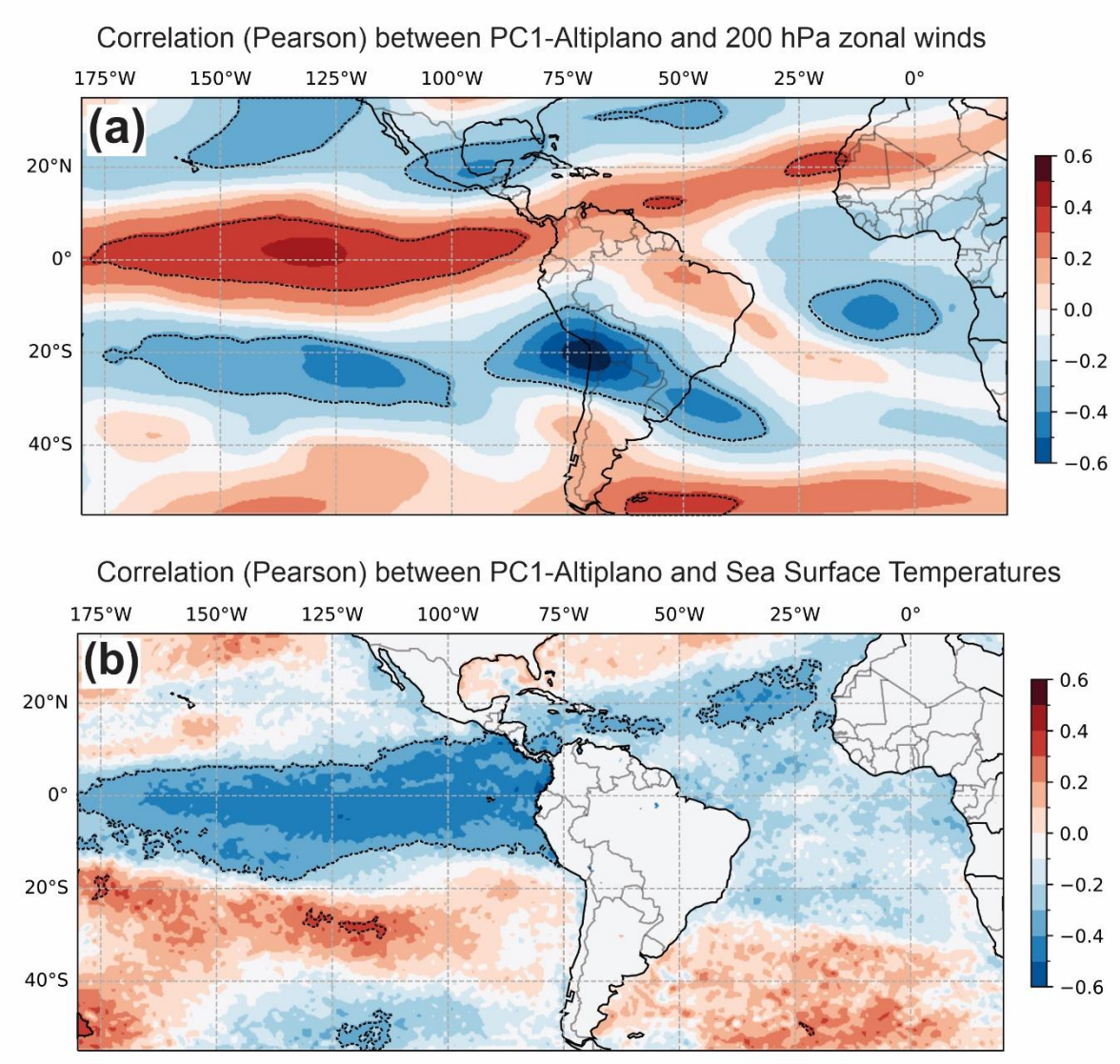

Figure S3. **(a)** Spatial correlation (Pearson) between the principal component of DJF precipitation variability in the southern Altiplano (PC1-Altiplano, see figure S4) and upper-level (200 hPa) zonal winds. **(b)** Spatial correlation (Pearson) between the principal component of DJF precipitation variability in the southern Altiplano and SSTs in the Pacific and Atlantic basins. Dashed black contours in (a) and (b) mark regions with significant correlation indexes ($p<0.01$). All atmospheric and oceanic data correspond to ERA5 reanalysis.

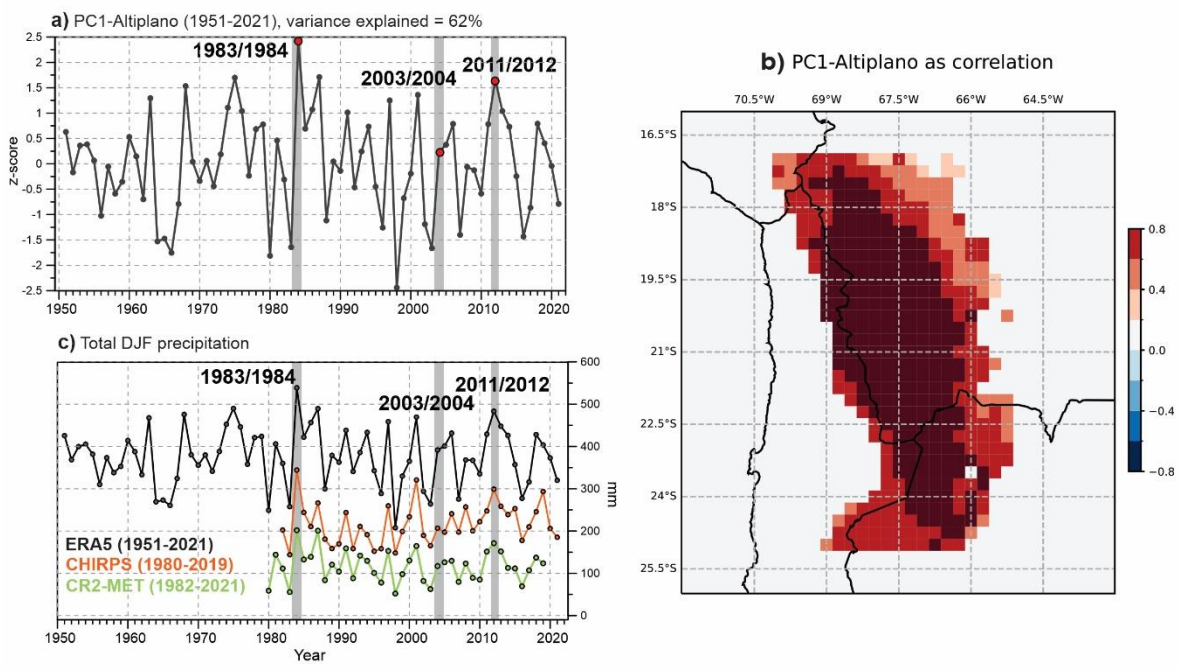

Figure S4. Historical DJF precipitation variability in the southern Altiplano. **(a)** The first principal component associated with the leading mode of DJF precipitation variability (PC1-Altiplano). PC1-Altiplano was calculated with an Empirical Orthogonal Function (EOF) analysis on the ERA5 reanalysis data over the 1951-2021 period (Segura et al., 2020). The EOF method was based on monthly means of "total precipitation" data at surface level, extracted for a sub-region limited to 17 and 25°S of latitude and 70 and 65°W of longitude from ERA 5 reanalysis data (Hersbach et al., 2019). All points of the grids below 3500 m.a.s.l. were removed. Reanalysis data was normalized using the whole interval mean and standard deviation (z-scores) to counterweight the strong moisture differences existing across the southern Altiplano. The grey vertical bands denote the DJF seasons selected as boundary conditions for the modelling experiment. **(b)** the PC1-Altiplano timeseries depicted as a correlation (Pearson) with the ERA5 DJF precipitation variability in the southern Altiplano region. The PC1-Altiplano shows strong positive correlations with total summertime precipitation over the entire southern Altiplano, indicating that it represents well DJF variability in the region. **(c)** PC1-Altiplano compared with the total DJF precipitation obtained from the Climate Hazards Center InfraRed Precipitation with Station data (CHIRPS; green line) and the grilled precipitation dataset from CR2MET (orange line). CHIRPS datasets are freely available at https://data.chc.ucsb.edu/products/CHIRPS-2.0/; whereas CR2MET products can be freely downloaded at: https://www.cr2.cl/datos-productos-grillados/. ERA5 dataset were obtained from the European Centre for Medium-Range Weather Forecasts (ECMWF) (https://cds.climate.copernicus.eu/cdsapp#!/search?type=dataset).

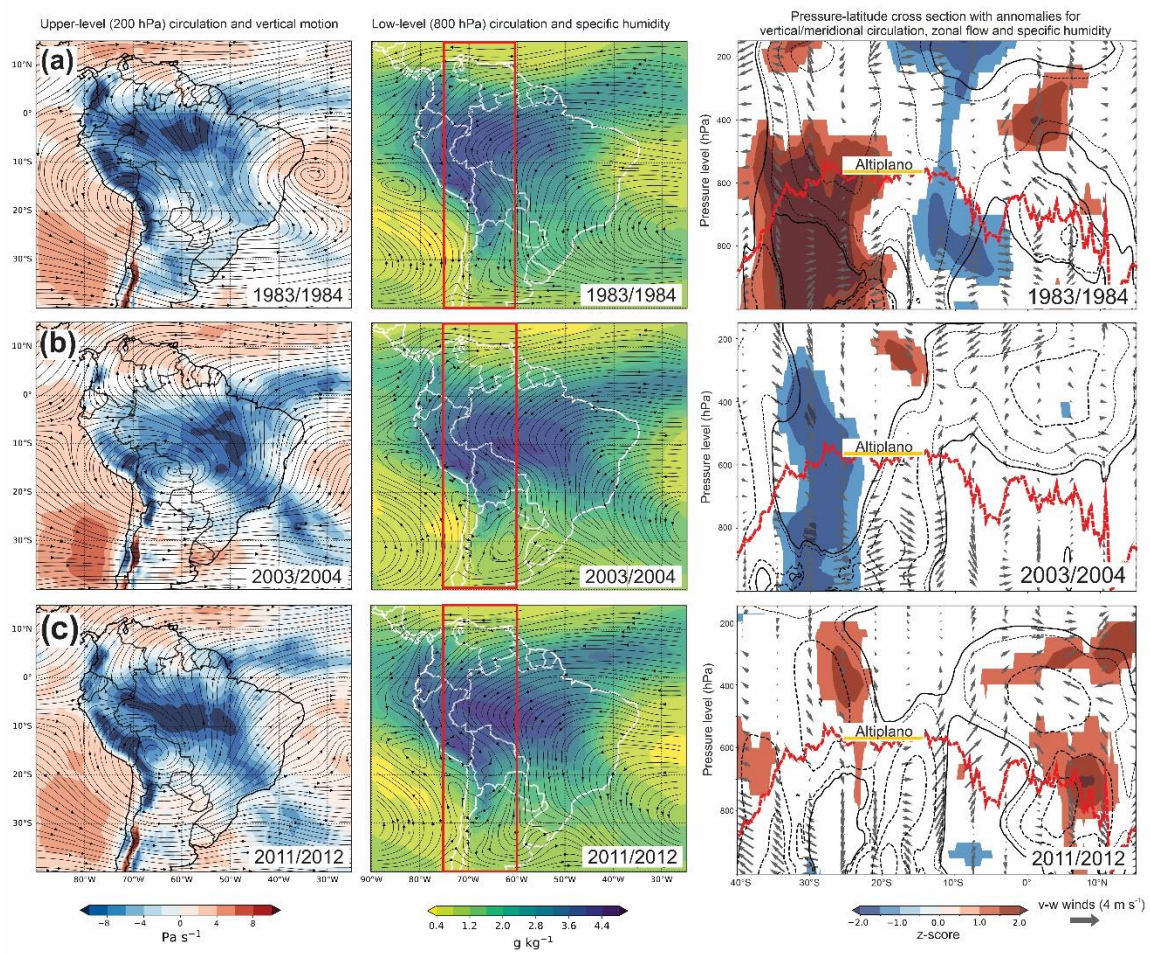

Figure S5. Composite plot with the tropospheric circulation and moisture transport for the 3 selected DJF periods used in the simulation experiment. **(a) Left panel**: Average (1983/1984, DJF) of vertical motion (w) at 500 hPa (colored; Pa s^{-1}) and integrated zonal and meridional winds (u,v) at 200 hPa (streamlines). Upward (downward) motion is depicted as negative blue (positive red) values. **Mid panel:** Average (1983/1984, DJF) of specific humidity (q) at 500 hPa (colored; g kg^{-1}) along with integrated zonal and meridional winds at 800 hPa (streamlines). **Right panel:** Pressure-latitude cross section showing the 1983/1984 DJF climate anomalies (z-score) relative to the 1951-2021 average. The plot includes the integrated vertical and meridional circulation (v,w; vectors; m s−1), zonal winds (u; contours) and specific humidity (q; shaded) anomalies. The longitudinal mean anomalies are calculated using v, w, u, and q in the region delimited by the red rectangle in the mid panel. Westerly (easterly) zonal anomalies are depicted as continuous (dashed) lines, with label at 4 m s-1 intervals. The dashed red line of the image represents the profile of maximum elevation of the Andes cordillera along the red rectangles in the mid panel. The position of the Altiplano is labelled in this figure. **(b)** same plots for the 2003/2004 DJF season. **(c)** same plots for the 2011/2011 DJF season. All atmospheric data correspond to ERA5 reanalysis.

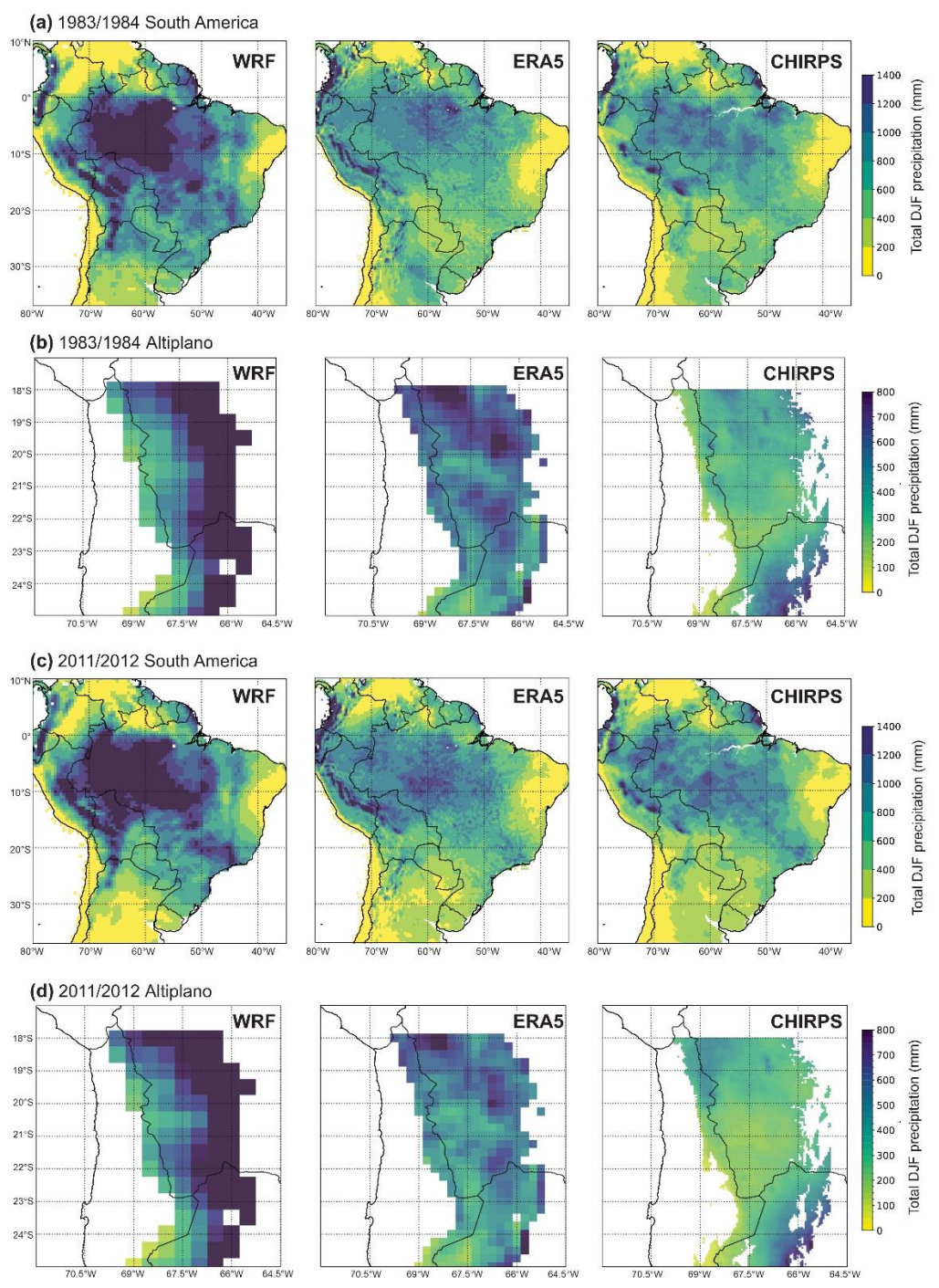

Figure S6. Comparison between the 1983/1984 and 2011/2012 summers in the WRF simulation, and the ERA5 reanalysis and the CHIRPS precipitation datasets. **(a) Left Panel**: total precipitation for the initial DJF period in the WRF 1983/1984 simulation. **Mid panel**: total 1983/1984 DJF precipitation in the ERA5 reanalysis. **Right panel**: total 1983/1984 DJF precipitation in the CHIRPS dataset. **(b)** Same as (a) for the southern Altiplano. **(c)** same as (a) but for the 2011/2011 DJF season. (d) Same as (b) but for the 2011/2012 DJF season.

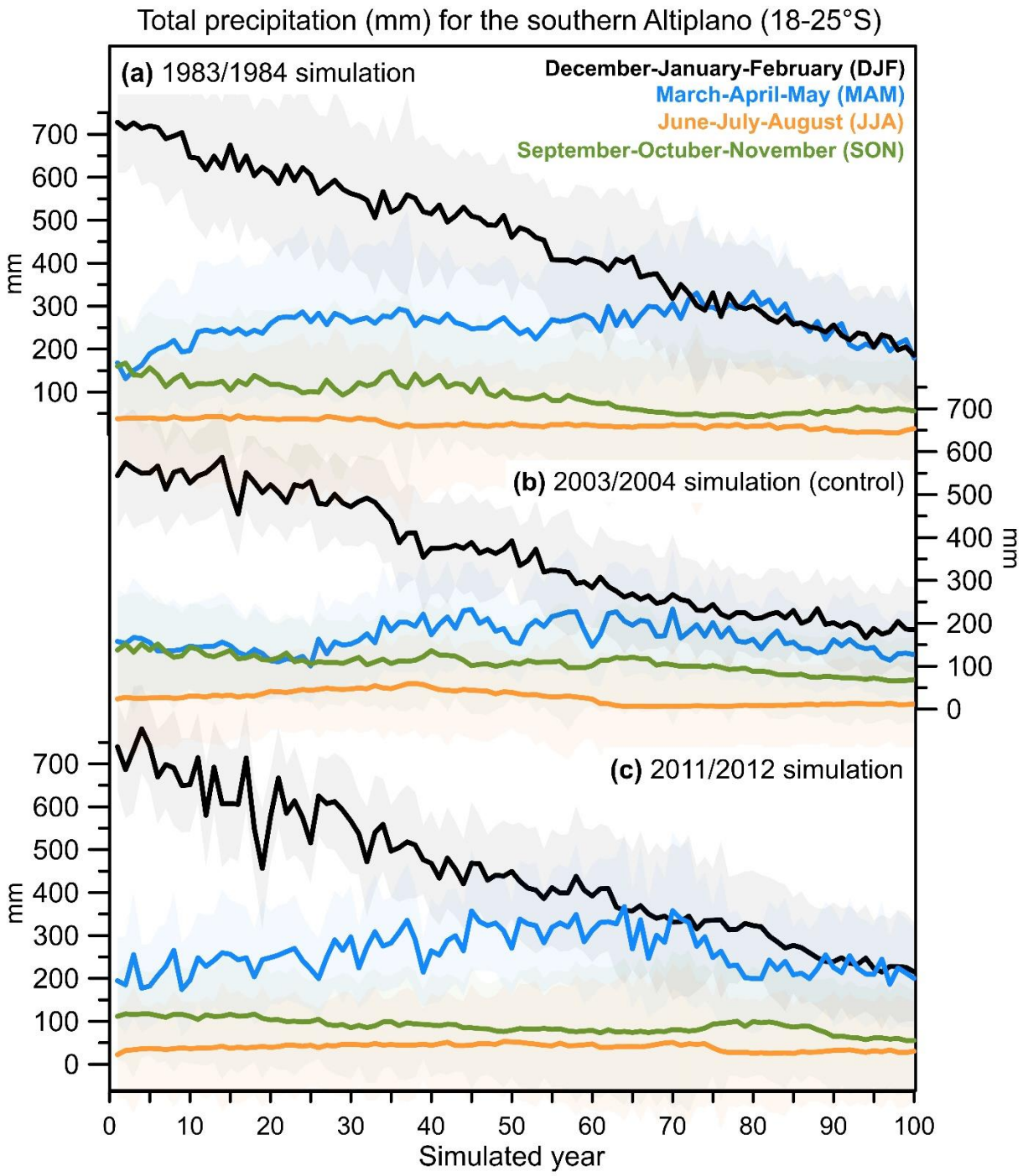

Figure S7. Total austral summer (December-January-February; DJF; black lines), autumn (March-April-May; MAM; blue), winter (June-July-August; JJA; yellow) and spring (September-October-November; SON; green) precipitation (mm) for the southern Altiplano, simulated in our three 100-yr WRF runs. The shading areas encompass one standard deviation from the regional mean.

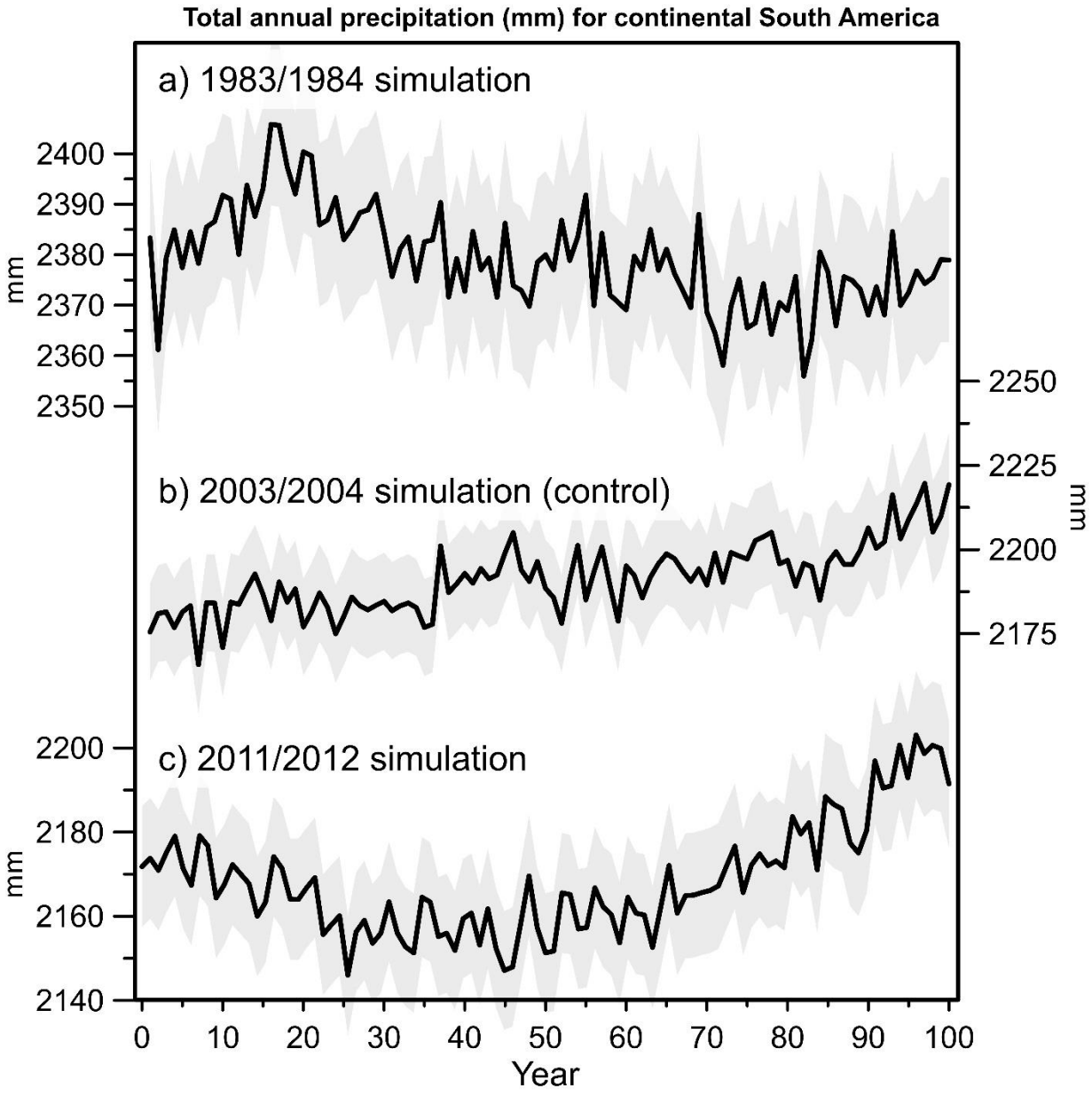

Figure S8. Total annual precipitation (mm) trends for continental South America (> 10 masl) in our three modeling simulations. The shading areas correspond to the 95% confidence interval for each precipitation.

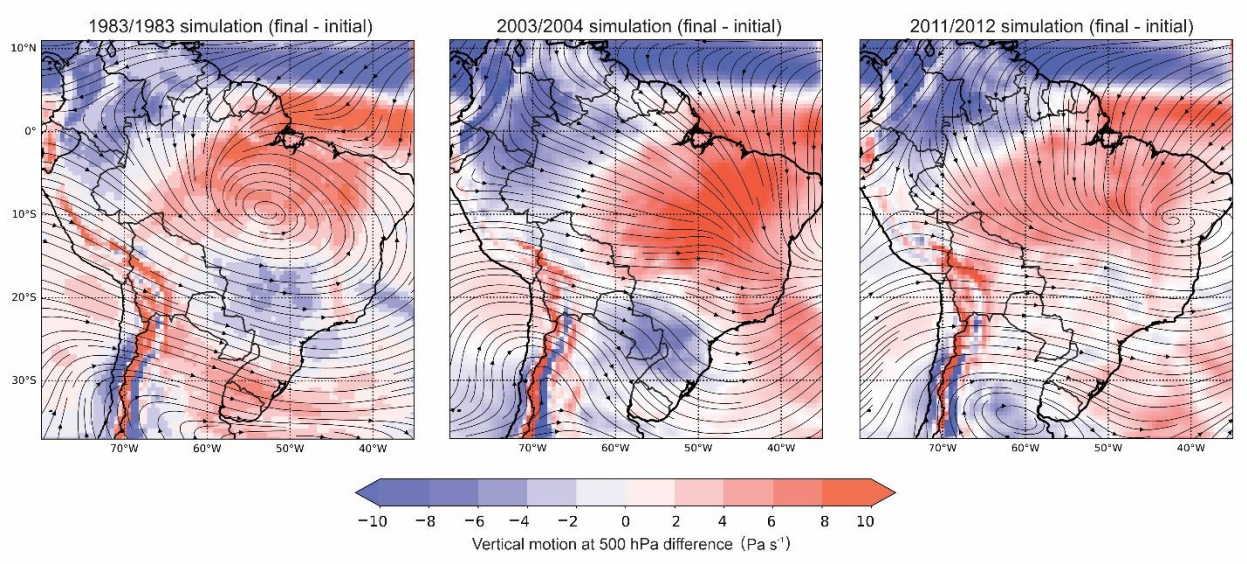

Figure S9. Differences between the averaged vertical motion (w) at 500 hPa (colored; Pa s−1) and integrated zonal and meridional winds (u,v) at 200 hPa (streamlines) between the final and initial decades of each simulation. Negative (positive) differences indicate increased upward (downward) motion in the final decade relative to the initial decade.

Model run	Initial date/time	Final date/time	Spin-up time	Number of cycles
1983/1984	10 November 1983, 09:00	10 November 1984, 06:00	10 days	100
2003/2004	2 May 2003, 15:00	2 May 2004, 12:00	10 days	100
2011/2012	21 June 2011, 09:00	21 June 2012, 06:00	12 days	100

Table S1. Initial and final date for the three WRF simulations presented in the article.

References

Berg, L.K., Zhong, S., 2005. Sensitivity of MM5-simulated boundary layer characteristics to turbulence parameterizations. Journal of Applied Meteorology 44, 1467-1483.

Dudhia, J., 1989. Numerical study of convection observed during the winter monsoon experiment using a mesoscale two-dimensional model. Journal of Atmospheric Sciences 46, 3077-3107.

Hersbach, H., Bell, B., Berrisford, P., Hirahara, S., Horányi, A., Muñoz-Sabater, J., Nicolas, J., Peubey, C., Radu, R., Schepers, D.J.Q.J.o.t.R.M.S., 2020. The ERA5 global reanalysis. 146, 1999-2049.

Hong, S.-Y., Lim, K.-S.S., Lee, Y.-H., Ha, J.-C., Kim, H.-W., Ham, S.-J., Dudhia, J., 2010. Evaluation of the WRF double-moment 6-class microphysics scheme for precipitating convection. Advances in Meteorology 2010.

Hooper, J., Marx, S.K., May, J.-H., Lupo, L.C., Kulemeyer, J.J., Pereira, E.d.l.Á., Seki, O., Heijnis, H., Child, D., Gadd, P., 2020. Dust deposition tracks late-Holocene shifts in monsoon activity and the increasing role of human disturbance in the Puna-Altiplano, northwest Argentina. The Holocene 30, 519-536.

Huang, M., Huang, B., Huang, A.H.-L., 2014. Implementation of the 5-layer thermal diffusion scheme in weather research and Forecasting model with Intel many integrated core (MIC) architecture, High-Performance Computing in Remote Sensing IV. SPIE, pp. 67-75.

Jara, I.A., Maldonado, A., de Porras, M.E., 2020. Late Holocene dynamics of the south American summer monsoon: New insights from the Andes of northern Chile (21° S). Quaternary Science Reviews 246.

Jara, I.A., Maldonado, A., González, L., Hernández, A., Sáez, A., Giralt, S., Bao, R., Valero Garcés, B.L., 2019. Centennial-scale precipitation anomalies in the southern Altiplano (18° S) suggest an extratropical driver for the South American summer monsoon during the late Holocene. Climate of the Past 15, 1845-1859.

Kain, J.S., 2004. The Kain–Fritsch convective parameterization: an update. Journal of applied meteorology 43, 170-181.

Kock, S.T., Schittek, K., Wissel, H., Vos, H., Ohlendorf, C., Schäbitz, F., Lupo, L.C., Kulemeyer, J.J., Lücke, A., 2019. Stable oxygen isotope records (δ18O) of a high-Andean cushion peatland in NW Argentina (24° S) imply South American Summer Monsoon related moisture changes during the Late Holocene. Frontiers in Earth Science 7, 45.

Mlawer, E.J., Taubman, S.J., Brown, P.D., Iacono, M.J., Clough, S.A., 1997. Radiative transfer for inhomogeneous atmospheres: RRTM, a validated correlated-k model for the longwave. Journal of Geophysical Research: Atmospheres 102, 16663-16682.

Schumacher, V., Fernández, A., Justino, F., Comin, A., 2020. WRF high resolution dynamical downscaling of precipitation for the Central Andes of Chile and Argentina. Frontiers in Earth Science 8, 328.

Segura, H., Espinoza, J.-C., Junquas, C., Lebel, T., Vuille, M., Garreaud, R., 2020. Recent changes in the precipitation-driving processes over the southern tropical Andes/western Amazon. Clim Dyn, 1-19.

Skamarock, W.C., Klemp, J.B., Dudhia, J., Gill, D.O., Barker, D.M., Duda, M.G., Huang, X.-Y., Wang, W., Powers, J.G., 2008. A description of the advanced research WRF version 3. NCAR technical note 475, 113.